Generating synthetic data to train a deep unrolled network for Hyperspectral Unmixing

Rassim Hadjeres, Christophe Kervazo, Florence Tupin

To cite this version:

Rassim Hadjeres, Christophe Kervazo, Florence Tupin. Generating synthetic data to train a deep unrolled network for Hyperspectral Unmixing. EUSIPCO 2024 : The 32nd edition European Signal Processing Conference, Aug 2024, Lyon, France. hal-04685198

HAL Id: hal-04685198

https://telecom-paris.hal.science/hal-04685198v1

Submitted on 5 Sep 2024

Generating synthetic data to train a deep unrolled network for Hyperspectral Unmixing

Rassim Hadjeres Christophe Kervazo Florence Tupin
LTCI, Télécom Paris, Institut Polytechnique de Paris
91120 Palaiseau, France.
Email: {name.surname}@telecom-paris.fr

***Abstract*—Hyperspectral unmixing is an essential tool for analyzing hyperspectral data, especially in remote sensing. Many approaches have been developed for this problem, ranging from model-based to deep learning-based, and (hybrid) unrolled methods. However, the development of supervisedly trained deep learning-based unmixing methods is hindered by the lack of available labeled training datasets. In this paper, to enable the supervised training of neural networks for hyperspectral unmixing, we propose a methodology to construct a synthetic training database directly from the hyperspectral image to unmix. We use this data generation approach to train an unrolled unmixing method LPALM. The trained LPALM is assessed on two real hyperspectral datasets and shows the best performances compared to other classical, unrolled, and autoencoder-based unmixing methods. The code of this work will be available at https://github.com/rhadjeres/Synthetic-Data-Generation-HSU.git.**

***Index Terms*—Hyperspectral unmixing, Synthetic training, Unrolled neural networks, Deep learning.**

I. INTRODUCTION

HYPERSPECTRAL (HS) imaging is an optical technology enabling to capture scenes in hundreds to thousands of narrow and contiguous spectral bands, covering a large wavelength range going from the visible to the near infrared and shortwave infrared. It has been applied to several domains such as medical imaging [1], astrophysics [2], and remote sensing [3]. The rich spectral information provided by hyperspectral images (HSIs) allows to finely characterize the spectral signatures of the materials present on a given scene. Nevertheless, a trade-off between spatial and spectral resolution is operated on the HS sensors to maintain acceptable signal-to-noise ratios, resulting in a lower spatial resolution compared to other remote sensing modalities such as multispectral or panchromatic imaging, limiting their ability to resolve fine-scale features on the ground. Thus, HS pixels usually correspond to mixtures of reflectance spectra of more than one distinct material present in the scene.

To facilitate the analysis of HSIs, hyperspectral unmixing (HSU) aims to decompose each pixel into p pure spectra, called *endmembers*, and their corresponding relative concentration inside of the pixel, called *abundances*. The simplest mixture model being the linear mixing model (LMM), which assumes each pixel to be a convex linear combination of the pure materials' endmembers present in the scene. Several methods have been developed to perform HSU under the LMM assumption, varying from iterative mathematical methods (geometrical, statistical, and sparse regression-based approaches) [5] to deep learning-based methods [6], and deep unrolled networks [7].

Model-based methods offer a clearly interpretable modeling of the unmixing process but often suffer from a high computational complexity and cumbersome hyper-parameters tuning. On the other hand, despite their high performance, deep learning-based methods may lack of interpretability due to their black-box nature. Deep unrolled networks try to combine the best from both worlds by offering efficient hybrid interpretable neural networks, where each iteration of an algorithm is recast into a layer of a neural network with learnable parameters.

Compared to other computer vision tasks, the development of deep-learning based methods for HS imaging, and especially HSU, is limited by the lack of available ground truth data. Indeed, image annotation can be very time-consuming and may require extensive fieldwork or laboratory analysis.

Contributions This paper proposes a methodology to construct a synthetic labeled database for training deep learning-based HSU methods, directly from the HSI to unmix. The methodology is then used to train an unrolled neural network LPALM with the aim to unmix real HS datasets. The performance of the supervisedly trained LPALM is then compared to two unsupervised classical algorithms, two unrolled methods, and an autoencoder-based method.

The remainder of this paper is organized as follows. Section II provides a brief reminder about the HSU problem, the PALM algorithm and its unrolled version LPALM. Section III is dedicated to the proposed data generation methodology. Section IV presents the results of the trained LPALM over two real datasets in comparison to other HSU methods. Finally, conclusion and future works are presented in section V.

II. BACKGROUND

A. Problem statement

According to the LMM, each pixel writes $x_n = As_n + e_n \in \mathbb{R}^L$ with $A \in \mathbb{R}^{L \times p}$ is the endmember matrix, L is the number of spectral bands, p is the number of pure materials present in the scene, $s_n \in \mathbb{R}^p$ is an abundance vector, and e_n is an additive Gaussian noise. The whole image writes $X = AS + E \in \mathbb{R}^{L \times N}$ where $S \in \mathbb{R}^{p \times N}$ is the abundance matrix, N is the number of pixels, and $E \in \mathbb{R}^{L \times N}$ is an additive Gaussian noise matrix. Due to the ill-posedness of the unmixing problem, regularization functions are necessary to avoid spurious solutions, and constrain the solution of the problem to be physically meaningful. Considering regularization functions g and f, respectively on S and A, the unmixing problem thus translates into

$$\underset{A \in \mathbb{R}^{L \times p}, S \in \mathbb{R}^{p \times N}}{\operatorname{argmin}} \frac{1}{2} ||X - AS||_F^2 + g(S) + f(A), \tag{1}$$

where $||.||_F$ is the Frobenius norm.
Usually, the endmembers are subject to the non-negativity constraint (ENC), while abundances are often subject to non-negativity (ANC) and sum-to-one constraints (ASC), i.e the abundances should lie in a probability simplex $\{s_n \in \mathbb{R}^p | s_{n,j} \geq 0, \sum_{j=1}^{p} s_{n,j} = 1\}$.

B. LPALM algorithm

Because not all the endmembers are present in each pixel of the HSI, it is relevant to impose sparse regularization. A possible formulation for the problem is

$$\underset{A \in \mathbb{R}^{L \times p}, S \in \mathbb{R}^{p \times N}}{\operatorname{argmin}} \frac{1}{2} ||X - AS||_F^2 + \lambda ||S||_1 + \underset{\{A^i, ||A^i||_2^2 \leq 1, i \in [1,p]\}}{\iota(\mathrm{A})} \tag{2}$$

where A^i is the i-th column of A, the l_1 norm encourages sparsity on the abundances S, and the oblique constraint encourages normalization of the columns of A to avoid degenerate solutions.

A popular optimization algorithm to solve problem (2) is the Proximal Alternating Linearized Minimization (PALM) algorithm [12], particularly appealing for its mathematical guarantees. It operates in an alternated framework according to the following iterations

$$\begin{aligned} S^{(k+1)} &= ST_{\theta^{(k)}} \left(S^{(k)} - \frac{1}{L_S^{(k)}} A^{(k)T} \left(A^{(k)} S^{(k)} - X \right) \right) \\ A^{(k+1)} &= \Pi_{||.||_2 \leq 1} \left(A^{(k)} - \frac{1}{L_A^{(k)}} \left(A^{(k)} S^{(k+1)} - X \right) S^{(k+1)T} \right) \end{aligned} \tag{3}$$

where (k) stands for the k^{th} iteration, $ST_{(.)}(.)$ is the soft thresholding operator, $\frac{1}{L_S^{(k)}}$ and $\frac{1}{L_A^{(k)}}$ respectively the gradient steps for $S^{(k)}$ and $A^{(k)}$, and $\theta^{(k)} = \frac{\lambda}{L_S^{(k)}}$ the thresholding parameter. However, similarly to other iterative algorithms, PALM may suffer from cumbersome hyperparameter tuning and a high computational complexity.

To overcome the above cited limitations, the authors of [13] proposed the LPALM as an unrolled version of PALM algorithm to solve problem (2) in the context of astrophysical data. LPALM recasts each iteration of PALM into a layer of a neural network according to the scheme

$$\begin{aligned} S^{(k+1)} &= ST_{\underline{\theta^{(k)}}} \left(S^{(k)} - \underline{W}^{(k)T} (A^{(k)} S^{(k)} - X) \right) \\ A^{(k+1)} &= \Pi_{||.||_2 \leq 1} \left(A^{(k)} - \frac{1}{\underline{L_A}^{(k)}} (A^{(k)} S^{(k+1)} - X) S^{(k+1)T} \right) \end{aligned} \tag{4}$$

where the thresholding parameter $\theta^{(k)}$, the matrix $W^{(k)T} = \frac{1}{L_S^{(k)}} A^{(k)T}$ and $L_A^{(k)}$, all underlined in (4), are parameters learned from the training process.

LPALM is trainable in a supervised fashion, given a training dataset $\{(X_i, A_i, S_i)\}_{i=1}^{N_{train}}$, according to the loss

$$Loss = \frac{1}{N_{train}} \sum_{i=1}^{N_{train}} \left(\frac{||\hat{S}_i - S_i||_F^2}{||S_i||_F^2} + \frac{||\hat{A}_i - A_i||_F^2}{||A_i||_F^2} \right), \tag{5}$$

where each X_i is a training image, A_i and S_i the associated ground truths, whereas $\hat{A}_i$ and $\hat{S}_i$ are the corresponding estimations of the algorithm. LPALM showed interesting results on synthetic realistic data, where the corresponding training data were generated according to a simulator.

In our work, we consider a variation of the LPALM replacing the soft thresholding operator by a ReLU(.) function, and a normalizing step on the columns of S enforcing ASC.

III. GENERATING SYNTHETIC LABELED DATA FOR HYPERSPECTRAL UNMIXING

In real life scenarios, especially in remote sensing, it is very difficult to have access to labeled training data or simulators, which hinders the applicability of LPALM and more generally supervisedly trained unmixing algorithms. In the sequel, we will present a three steps methodology to efficiently generate synthetic training samples directly from the image to unmix.

A. Spectral collection and augmentation

Our goal is to generate labeled training samples for hyperspectral unmixing. However, relying on ready-made libraries such as the USGS spectral library [21] may lead to library mismatch due to different acquisition conditions. Alternatively, we propose to construct spectral libraries directly from the observed images.

The first step of our methodology can be divided into:

1) Employing an endmember extraction algorithm (EEA) a predetermined number of time $N_{iterEEA}$ to extract different samples spectra of the pure materials.
2) Removing duplicates and Grouping spectra corresponding to each material using a clustering algorithm to construct a first spectral library Lib_{EEA}.
3) Augmenting the spectral library by applying perturbation functions that mimick spectral variability on the spectra, resulting in a new augmented library Lib_{Aug}.

We use the vertex component analysis (VCA) algorithm [8] to extract the spectra, and the Fuzzy c-means algorithm [14] to group them. VCA is interesting for its randomized nature, which permits to extract different endmember samples by running the algorithm several times. Nevertheless, there is some redundancy in the extracted endmembers limiting the number of available training spectra. The used perturbation procedure for augmentation has been introduced in [15], and consists in multiplying reference spectra from Lib_{EEA} by randomly generated piece-wise affine functions. After some level of variability c_{var} is fixed by the user, piece-wise affine functions are generated according to four parameters:

- $\xi_i \sim \mathcal{U}_{[1-c_{var}/2, 1+c_{var}/2]}$ $\forall i \in \{1,2,3\}$.
- $L_{break} = \lfloor \lfloor L/2 \rfloor + \lfloor LU/3 \rfloor \rfloor \in \{1, ..., L\}$ is the spectral band marking the non-linearity and $U \sim \mathcal{N}(0,1)$.

An illustration of a randomly generated piece-wise affine function and augmented spectra are respectively illustrated in Fig. 1 and Fig. 2.

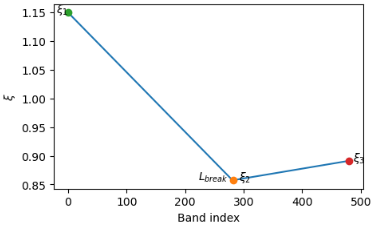

Fig. 1. An example of randomly generated piecewise affine function.

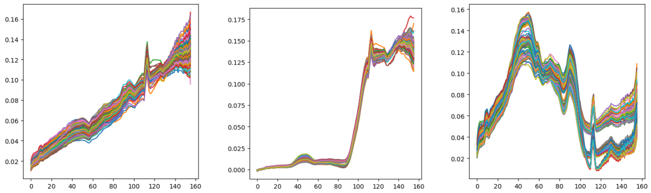

Fig. 2. Augmented spectra for Samson dataset (cf. Section IV), of respectively, from left to right, soil, tree and water materials signatures with $c_{var} = 0.4$.

B. Abundance maps generation

Abundance maps also play an important role when generating synthetic labeled hyperspectral images. This step of our methodology can be divided into:

1) Computing a reference endmember matrix A_{ref} by taking the average spectrum from Lib_{EEA} associated to each material.
2) Estimating a reference abundance map S_{ref} by applying a fully constrained least squares procedure on the hyperspectral image to unmix and A_{ref}.
3) Estimating the parameters of a statistical distribution associated to S_{ref} in order to generate samples following the same distribution.

S_{ref} is obtained using the fully constrained least squares unmixing (FCLSU) algorithm [19]. We use Dirichlet mixtures as a prior for abundance maps [16], [17]. On one hand, the Dirichlet distribution is well suited to model fractions and ensures non-negativity and sum-to-one constraints of the abundances. On the other hand, mixtures allow one to model complex distributions in which the mass probability is scattered inside the simplex.

Precisely, the Dirichlet mixtures distribution writes as

$$p_S(s_n|\theta) = \sum_{q=1}^{M} \epsilon_q D(s_n|\theta_q) = \sum_{q=1}^{M} \epsilon_q \frac{\Gamma(\sum_{j=1}^{p} \theta_{qj})}{\prod_{j=1}^{p} \Gamma(\theta_{qj})} \prod_{j=1}^{p} s_{n,j}^{\theta_{qj}-1} \quad (6)$$

where $\Gamma(.)$ denotes the gamma function, M is the number of modes, ϵ_q and $D(s_n|\theta_q)$ respectively denote the probability of mode q and its Dirichlet density parameterized by $\theta_q \equiv \{\theta_{q1}, ..., \theta_{qp}\}$. The complete set of parameters is denoted as $\theta \equiv \{\epsilon_1, ..., \epsilon_M, \theta_1, ..., \theta_M\}$. The parameters are estimated by maximizing the associated log-likelihood according to a specific Expectation-Maximization (EM) algorithm [18]. The log-likelihood writes

$$\mathcal{L}(\theta) = \sum_{n=1}^{N} [\sum_{q=1}^{M} z_q^{(n)} \log(\epsilon_q D(s_n|\theta_q))] \quad (7)$$

where $z^{(n)} = [z_1^{(n)}, ..., z_M^{(n)}]$ is a binary vector of size M with a unique value $z_q^{(n)}$ of one, indicating the mode of the n-th sample. The number of modes is determined using the Akaike information criterion (AIC). The EM algorithm alternates between the E-step and the M-step.

- **E-step:** Given the samples $\{s_n\}_{n=1}^{N}$ and the current estimated parameter $\hat{\theta}^{(k)}$, this step consists in computing the conditional expectation of the complete log-likelihood

$$Q(\theta; \hat{\theta}^{(k)}) = \sum_{n=1}^{N} [\sum_{q=1}^{M} \beta_q^{(n,k)} \log(\epsilon_q D(s_n|\theta_q))] \quad (8)$$

where

$$\beta_q^{(n,k)} = \mathbb{E}[z_q^{(n)}|\hat{\theta}_q^{(k)}] = \frac{\hat{\epsilon}_q^{(k)} D(s_n|\hat{\theta}_q^{(k)})}{\sum_{l=1}^{M} \hat{\epsilon}_l^{(k)} D(s_n|\hat{\theta}_l^{(k)})}. \quad (9)$$

- **M-step:** This step updates the parameters

$$\begin{aligned} \hat{\epsilon}_q^{(k+1)} &= \frac{1}{N} \sum_{n=1}^{N} \beta_q^{(n,k)}, \\ \hat{\theta}_{qj}^{(k+1)} &= \Psi^{-1}\left(\Psi\left(\sum_{l=1}^{p} \hat{\theta}_{ql}^{(k)}\right) + \frac{\sum_{n=1}^{N} [\beta_q^{(n,k)} \log(s_{n,j})]}{\sum_{n=1}^{N} \beta_q^{(n,k)}}\right) \end{aligned} \quad (10)$$

with $\Psi(x) \equiv d(\log\Gamma(x))/dx$ the psi(.) function and $\Psi^{-1}(.)$ its inverse.

Illustrations of the estimated density parameters on three abundance materials are given in Fig. 3.

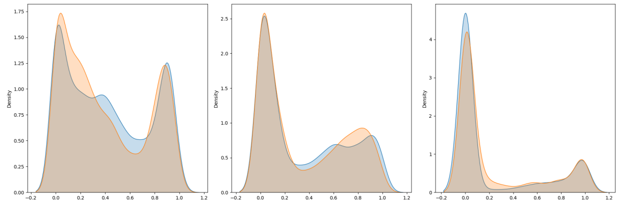

Fig. 3. Reference empirical density (Blue) and associated estimated Dirichlet mixtures density (Orange) of respectively soil, tree and water materials associated to Samson dataset.

C. Labeled hyperspectral samples

The final stage consists in generating mixed hyperspectral samples. Each training sample corresponds to a tuple $\{(X_i, A_i, S_i)\}_{i=1}^{N_{train}}$, where A_i is an endmember matrix sampled from Lib_{Aug}, S_i is an abundance map sampled from the estimated Dirichlet mixture distribution, and $X_i = A_i S_i + E_i$ is a mixed hyperspectral sample with E_i an additive gaussian noise such that $SNR = 30\text{dB}$.

IV. EXPERIMENTS

In this section, we assess the unmixing performance of the supervisedly trained LPALM on two real-world datasets, in comparison with other unmixing methods, namely: VCA [8] combined with FCLSU [19], SNPA [9], DNMF-net [10], SNMF-Net [11], and CNNAEU [20]. Among these compared methods, VCA (+FCLSU) and SNPA are geometric unsupervised methods, while DNMF-Net and SNMF-Net are two unrolled NMF-based methods. DNMF-Net unrolls a multiplicative update algorithm, SNMF-Net unrolls an L_p-NMF algorithm where the parameter p is learned from the data, and both algorithms are unsupervisedly trained thanks to a reconstruction loss. And finally, CNNAEU is an autoencoder-based unmixing method that has shown highly accurate results in the critical comparison of autoencoder-based unmixing methods [22]. All relevant parameters of these approaches have been set as suggested in their original implementation.

The spectral angle distance (SAD) and the root-mean-square error (RMSE) were used in order to quantitatively compare the performance of the algorithms. SAD measures the dissimilarity between a reference endmember A_r and its associated estimation $\hat{A}_r$, and is defined as

$$SAD_r = \arccos\left(\frac{\mathbf{A}_r^T\hat{\mathbf{A}}_r}{\|\mathbf{A}_r\|\|\hat{\mathbf{A}}_r\|}\right). \tag{11}$$

RMSE computes the error between a reference abundance map S_r and its associated estimated map $\hat{S}_r$, it is defined as

$$RMSE_r = \left(\frac{1}{N}\|\mathbf{S}_r - \hat{\mathbf{S}}_r\|^2\right)^{\frac{1}{2}} \tag{12}$$

where N is the number of elements of the abundance map. The smaller the values of SAD and RMSE, the better the unmixing.

Columns of all the hyperspectral images and mixing matrices used in the experiments are normalized to get rid of scaling factors, and the variability controlling parameter c_{var} has been set to 0.4 for all the experiments. The number of layers of LPALM was set to 5, initialized with A_{ref} and S_{ref}, and it was trained on 100 generated training samples of the same dimension as the ground truth matrices with Adam optimizer and a learning rate $lr = 10^{-6}$ during 600 epochs.

Samson Dataset contains 95×95 pixels, and 156 channels covering the spectral range of 400nm-900nm. We considered three main endmembers present in the scene including water, soil and tree.

Table I provides endmember estimation results of all the compared methods w.r.t SAD. It shows that LPALM outpeforms the other methods on average SAD, when estimating Soil and Tree endmembers, and places second closely after SNPA for Water endmember. In comparison with the other methods, SNMF-Net not only shows the worst endmembers results, but also the worst abundance estimation results overall according to table II. Even if both SNMF-Net and DNMF-Net are unrolled networks relying on a reconstruction loss, DNMF-Net performs better as it uses 70% of the image as training pixel while SNMF-Net uses only 500 pixels i.e. around 6% here. LPALM still peforms the best on average RMSE and for the Soil abundance, and places second for Tree and Water abundances.

Jasper ridge Dataset contains 100×100 pixels, and 224 channels covering the spectral range of 380nm-2500nm. To mitigate the water absorption and atmosphere effects, noisy bands (1–3, 108–112, 154–166, and 220–224) have been removed, leading to 198 remaining bands. We considered four main endmembers which are tree, water, road and soil.

According to table III, LPALM exhibits the best endmember estimation on average for Tree and Road materials, and places second for Soil closely after VCA which performs on average three times better than SNPA on this dataset. This shows that the theoretical conditions that guarantee the results of SNPA to be correct are not verified in practice. The endmember estimation error of SNPA also propagates to abundances as shown in table IV. Once again, SNMF-Net and CNNAEU show the worst results for abundance estimation while LPALM performs the best. This shows the efficiency and utility of efficiently generated synthetic training datasets.

TABLE I
SAD RESULTS ON SAMSON DATASET.

Algorithm	VCA	SNPA	DNMF	SNMF	CNNAEU	LPALM
Soil	0.0236	0.0404	0.0233	0.0713	0.0323	**0.0152**
Tree	0.0417	0.0753	0.0494	0.1112	0.0418	**0.0356**
Water	0.1655	**0.0326**	0.0368	0.2164	0.0959	0.0361
Mean	0.0769	0.0494	0.0365	0.1330	0.0567	**0.0290**

TABLE II
RMSE RESULTS ON SAMSON DATASET.

Algorithm	FCLSU	SNPA	DNMF	SNMF	CNNAEU	LPALM
Soil	0.0591	0.0790	0.0813	0.5704	0.2446	**0.0498**
Tree	**0.0346**	0.0627	0.0774	0.5661	0.2471	0.0368
Water	0.0525	**0.0254**	0.0393	0.4520	0.2283	0.0271
Mean	0.0487	0.0557	0.0660	0.5295	0.2400	**0.0379**

TABLE III
SAD RESULTS ON JASPER DATASET.

Algorithm	VCA	SNPA	DNMF	SNMF	CNNAEU	LPALM
Tree	0.0638	0.1627	0.0353	0.3413	0.0774	**0.0200**
Water	0.1437	0.0751	0.1645	0.3852	**0.0534**	0.1068
Soil	**0.1179**	0.2304	0.1632	0.1696	0.1323	0.1218
Road	0.0901	0.6988	0.0975	0.0836	0.1101	**0.0284**
Mean	0.1039	0.2918	0.1151	0.2449	0.0933	**0.0693**

TABLE IV
RMSE RESULTS ON JASPER DATASET.

Algorithm	FCLSU	SNPA	DNMF	SNMF	CNNAEU	LPALM
Tree	0.0832	0.1025	0.0629	0.5671	0.2911	**0.0617**
Water	**0.0788**	0.0893	0.1567	0.5250	0.2753	0.0938
Soil	0.1497	0.1894	0.1352	0.4715	0.4005	**0.1287**
Road	0.1283	0.2455	0.1826	0.5601	0.3053	**0.1244**
Mean	0.1100	0.1567	0.1344	0.5309	0.3180	**0.1021**

V. CONCLUSION

This paper proposed a synthetic data generation strategy allowing the use of LPALM algorithm in remote sensing hyperspectral unmixing. The trained LPALM showed better results compared to other state-of-the-art methods, highlighting the efficiency of the proposed methodology. Future work will include the assessment of this data generation methodology on other architectures.

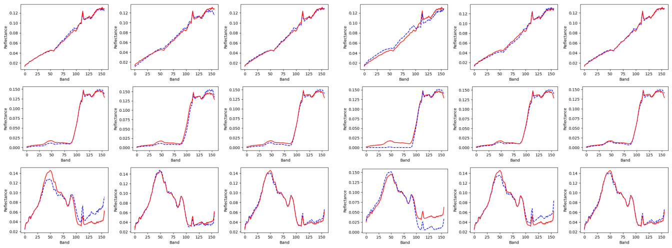

Fig. 4. Ground truth spectra (red) and associated estimated spectra (blue) of Samson dataset. From the top to the bottom: Soil, tree, and water. From left to right: VCA, SNPA, DNMF-Net, SNMF-Net, CNNAEU and LPALM.

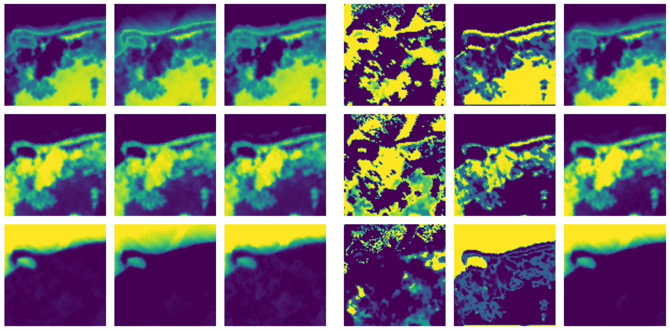

Fig. 5. Estimated abundance maps of Samson dataset. From the top to the bottom: Soil, tree, and water. From left to right: VCA, SNPA, DNMF-Net, SNMF-Net, CNNAEU and LPALM.

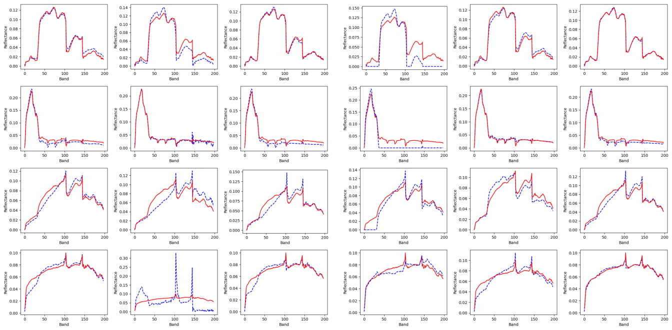

Fig. 6. Ground truth spectra (red) and associated estimated spectra (blue) of Jasper dataset. From the top to the bottom: Tree, Water, Soil and Road. From left to right: VCA, SNPA, DNMF-Net, SNMF-Net, CNNAEU and LPALM.

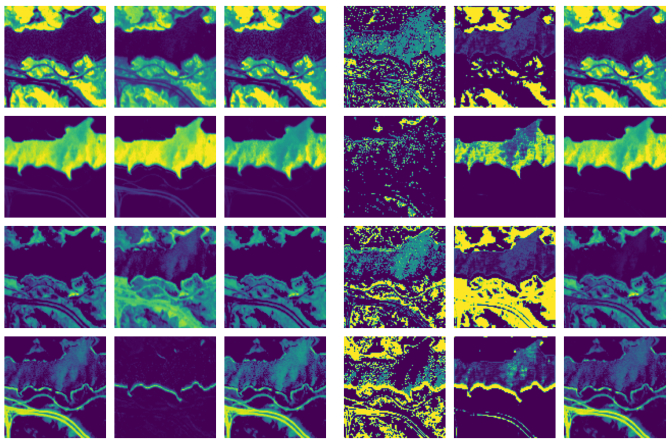

Fig. 7. Estimated abundance maps of Jasper dataset. From the top to the bottom: Tree, Water, Soil and Road. From left to right: VCA, SNPA, DNMF-Net, SNMF-Net, CNNAEU and LPALM.

REFERENCES

[1] G. Lu and B. Fei, "Medical hyperspectral imaging: A review," *Journal of Biomedical Optics*, vol. 19, no. 1, p. 010901, 2014.

[2] S. Moussaoui et al., "On the decomposition of Mars hyperspectral data by ICA and Bayesian positive source separation,". *Neurocomputing*, vol. 71 (10-12), pp. 2194-2208, Elsevier, 2008.

[3] J. M. Bioucas-Dias et al., "Hyperspectral Remote Sensing Data Analysis and Future Challenges," *IEEE Geoscience and Remote Sensing Magazine*, vol. 1, no. 2, pp. 6-36, June 2013.

[4] B. Rasti et al., "Image Processing and Machine Learning for Hyperspectral Unmixing: An Overview and the HySUPP Python Package," *IEEE Transactions on Geoscience and Remote Sensing*, vol. 62, pp. 1-31, 2024.

[5] J. M. Bioucas-Dias et al., "Hyperspectral Unmixing Overview: Geometrical, Statistical, and Sparse Regression-Based Approaches," *IEEE Journal of Selected Topics in Applied Earth Observations and Remote Sensing*, vol. 5, no. 2, pp. 354-379, April 2012.

[6] J. S. Bhatt and M. V. Joshi, "Deep Learning in Hyperspectral Unmixing: A Review," *IGARSS 2020 - 2020 IEEE International Geoscience and Remote Sensing Symposium*, Waikoloa, HI, USA, 2020, pp. 2189-2192.

[7] V. Monga, Y. Li and Y. C. Eldar, "Algorithm Unrolling: Interpretable, Efficient Deep Learning for Signal and Image Processing,". *IEEE Signal Processing Magazine*, vol. 38, no. 2, pp. 18-44, March 2021.

[8] J. M. P. Nascimento and J. M. Bioucas-Dias, "Vertex component analysis: A fast algorithm to unmix hyperspectral data," *IEEE Transactions on Geoscience and Remote Sensing*, vol. 43, no. 4, pp. 898–910, April 2005.

[9] N. Gillis. "Successive nonnegative projection algorithm for robust nonnegative blind source separation," *SIAM Journal on Imaging Sciences*, 7(2), 1420-1450. 2014.

[10] R. Nasser, Y. C. Eldar, and R. Sharan "Deep unfolding for non-negative matrix factorization with application to mutational signature analysis," *Journal of Computational Biology*, vol. 29 (1), pp. 45-55, 2022.

[11] F. Xiong et al., "SNMF-Net: Learning a deep alternating neural network for hyperspectral unmixing," *IEEE Transactions on Geoscience and Remote Sensing*, vol. 60, pp. 1-16, 2022.

[12] J. Bolte, S. Sabach, and M. Teboulle, "Proximal alternating linearized minimization for nonconvex and nonsmooth problems," *Mathematical Programming,* Ser A 146(1-2), 459-494, 2014.

[13] M. Fahes et al.,"Unrolling PALM for sparse semi-blind source separation," *International Conference on Learning Representations*, 2022.

[14] I. Gath, and Geva, A. B. "Unsupervised Optimal Fuzzy Clustering," *IEEE Transactions on Pattern Analysis and Machine Intelligence*, vol. 11, no. 7, July 1989.

[15] P. -A. Thouvenin, N. Dobigeon and J. -Y. Tourneret, "Hyperspectral Unmixing With Spectral Variability Using a Perturbed Linear Mixing Model," in *IEEE Transactions on Signal Processing,* vol. 64, no. 2, pp. 525-538, Jan.15, 2016.

[16] J. M. P. Nascimento and J. M. Bioucas-Dias, "Hyperspectral unmixing algorithm via dependent component analysis," in *IEEE International Geoscience and Remote Sensing Symposium*, Barcelona, Spain, 2007, pp. 4033-4036.

[17] J. M. P. Nascimento and J. M. Bioucas-Dias, "Hyperspectral Unmixing Based on Mixtures of Dirichlet Components," *IEEE Transactions on Geoscience and Remote Sensing,* vol. 50, no. 3, pp. 863-878, March 2012.

[18] T. Minka, "Estimating a Dirichlet distribution," MIT, Cambridge, MA, 2000. Technical Report.

[19] D. Heinz, C. -I. Chang, and M. L. G. Althouse, "Fully constrained least-squares based linear unmixing [hyperspectral image classification]," *IEEE 1999 International Geoscience and Remote Sensing Symposium,* IGARSS'99, Hamburg, Germany, 1999, pp. 1401-1403 vol.2.

[20] B. Palsson, M. O. Ulfarsson and J. R. Sveinsson, "Convolutional Autoencoder for Spectral–Spatial Hyperspectral Unmixing," *IEEE Transactions on Geoscience and Remote Sensing,* vol. 59, no. 1, pp. 535-549, Jan. 2021.

[21] R. Clark, et al. "Imaging spectroscopy: Earth and planetary remote sensing with the USGS Tetracorder and expert systems," *Journal of Geophysical Research: Planets,* vol. 108, no. E12, 2003.

[22] B. Palsson, M. O. Ulfarsson and J. R. Sveinsson, "Blind hyperspectral unmixing using autoencoders: A critical comparison," *IEEE Journal of Selected Topics in Applied Earth Observations and Remote Sensing,* vol. 15, pp. 1340-1372, 2022.